condensed matter

MDPI

Article

Atomristor Mott Theory of Sn Adatom Adlayer on a Si Surface

Luis Craco [1,*], Edson F. Chagas [1], Sabrina S. Carara [1] and Byron Freelon [2]

[1] Institute of Physics, Federal University of Mato Grosso, Cuiabá 78060-900, Brazil; efchagas@fisica.ufmt.br (E.F.C.); sabrina@fisica.ufmt.br (S.S.C.)
[2] Department of Physics and Texas Center for Superconductivity, University of Houston, Houston, TX 77204, USA; bkfreelon@uh.edu
* Correspondence: lcraco@fisica.ufmt.br

Abstract: We use a combination of density functional theory (DFT) and dynamical mean field theory (DMFT) to unveil orbital field-induced electronic structure reconstruction of the atomic Sn layer deposited onto a Si(111) surface (Sn/Si(111)$-\sqrt{3}\times\sqrt{3}R30°$), also referred to as α-Sn. Our DFT + DMFT results indicate that α-Sn is an ideal testing ground to explore electric field-driven orbital selectivity and Mott memory behavior, all arising from the close proximity of α-Sn to metal insulator transitions. We discuss the relevance of orbital phase changes for α-Sn in the context of the current–voltage ($I-V$) characteristic for future silicon-based metal semiconductor atomristors.

Keywords: Hubbard model; DFT + DMFT; metal–insulator transition; atomristor; current–voltage

1. Introduction

In recent years, significant progress has been achieved in discovering promising bulk and low-dimensional material candidates for the advancement of computational speed and efficiency in areas of big data analytics and artificial intelligence [1,2], neuromorphic computing [3,4], and pattern recognition and adaptive circuitry [5]. Of note, neuron-inspired computation is a paradigm that aims to mimic the biological brain for future hardware-oriented computing [6,7] in an energy efficient manner [8]. Particularly, since traditional CMOS circuitry made to implement neuromorphic computing faces challenges in power consumption and scalability [9], both memristors [3,4] (resistors with memory) and atomristors [10,11] (atomically thin or atomic sheet memristors) have been synthesized using predominantly transition metal oxide materials [1,2,12,13]. Volatile memristors display continuum current [14,15] values, with the monotonic hysteresis lobe area dependence on external voltage. Most nonvolatile [1,2,10,16] memristive systems are characterized by a discontinuos hysteresis loop in the current–voltage ($I-V$) characteristic and the shrinkage of the pinched hysteresis loop to a single value at large voltages [15]. Interestingly, these frequency-dependent responses have been studied and applied in the context of memristors and atomristors in view of nonvolately encoding switches for logic computing and data processing [11] as well as for communication platforms, including low-power internet of things (IoT) and mobile systems [1,2,16].

Nonvolatile resistance switching has been observed in various multilayer two-dimensional material morphologies, including pristine, reduced and functionalized graphene oxide mixtures, partially degraded black phosphorus, functionalized MoS_2, and transitional metal dichalcogenide-based hybrids [17,18], as well as in multilayer *h*-BN [19,20]. Importantly, in atomristors, the resistance can be modulated between a high-resistance and a low-resistance state and subsequently retained in the absence of a power supply [10]. However, it was believed that the nonvolatile resistive switching phenomenon might not be accessible in single-layer atomic sheets [21] due to excessive leakage current that prevents nanometre scaling in conventional oxide-based vertical metal–insulator–metal [10] configurations. With this caveats, ref. [10] was able to overcome

check for updates

Citation: Craco, L.; Chagas, E.F.; Carara, S.S.; Freelon, B. Atomristor Mott Theory of Sn Adatom Adlayer on a Si Surface. *Condens. Matter* **2024**, *9*, 32. https://doi.org/10.3390/condmat9030032

Academic Editor: Sergio Caprara

Received: 23 May 2024
Revised: 11 July 2024
Accepted: 24 July 2024
Published: 2 August 2024

this fundamental limitation by using atomic sheets of transition metal dichalcogenides. These, among other similar low-dimensional systems [1,2,22], are now collectively labeled as atomristors, displaying memristive effects [23] in atomically thin nanomaterials or in low-dimensional atomic sheets. Here, motivated by a tip-assisted phase switching in a Sn double-layer structure grown on a Si(111) surface [22], we focus our attention on the atomristor-like properties of α-Sn [24], i.e., a two-dimensional atomic Sn layer deposited onto a Si(111) surface (Sn/Si(111) $-\sqrt{3}\times\sqrt{3}R30^{\circ}$, see Figure 1), revealing that analog- and weakly digital-like Mott memory can be induced by tunneling polarity [22] or atomic-scaled orbital order [25] effects.

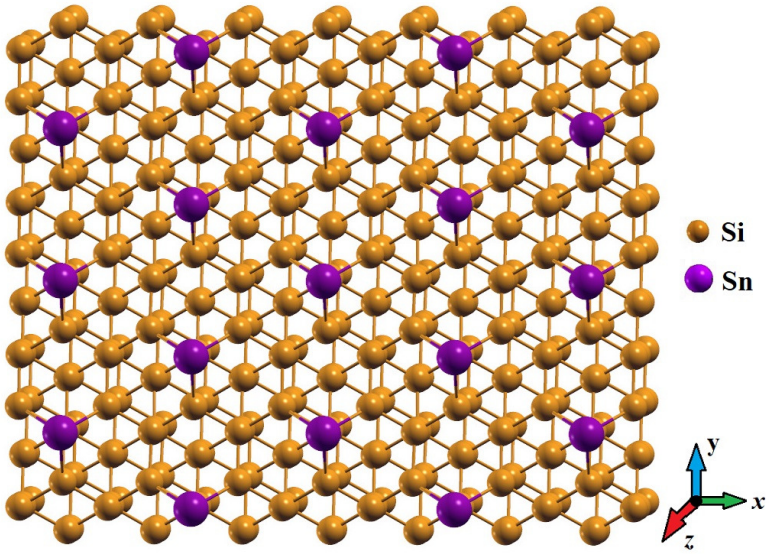

Figure 1. Top view of the atomic geometry of α-Sn, where the Sn atoms form a $\sqrt{3}\times\sqrt{3}R30^{\circ}$ superstructure relative to the 1×1 periodicity of the Si(111) surface. For contrast, the Sn (Si) atoms are drawn with dark/violet (bright/gold) circles.

Adsorption of group IV elements on semiconductor surfaces such as Si, Ge, or SiC [26–31] often promote intriguing charge and spin phases at the two-dimensional limit, including unconventional superconductivity [32,33], charge density waves [28,34–36], and unusual magnetism [37,38]. The triangular adlayer, the adatom lattice of α-Sn, provides a rich playground for the investigation and realization of correlated many-body physics [36,38–43], including the emergence of superconductivity ($T_c = 4.7 \pm 0.3$ K) [32] by employing heavily boron-doped Si substrates. A characteristic one-particle feature in the electronic structure of α-Sn is the presence of a narrow band with a mostly Sn-5p_z orbital character, which crosses the Fermi energy (E_F) and is well-separated from other bonding and anti-bonding bands emerging at high energies [39,43]. Apart from the narrow bandwidth, ($W \approx 0.45 \pm 0.05$ eV) [39,43] an additional interesting feature of the effective surface band in the semiconducting gap of α-Sn is the existence of a van Hove singularity located near 30 meV below E_F, suggesting an extended van Hove singularity scenario in α-Sn similar to that reported, for example, in doped graphene [44], bilayer cuprates [45], as well as in moiré materials near the van Hove filling [46].

Scanning tunneling [22,31,33,47,48] and spectroscopy [38,49] studies show that U-shaped gap features develop around E_F at small nanodomains going over to a V-shaped, pseudogap-like electronic state when the spectra are taken on different size domains induced via the modulation doping scheme [31,32,41,48]. Interestingly, ref. [48] revealed that a low-energy pseudogap feature that is rather stable against the application of external magnetic fields but can progressively be depleted via thermal broadening with increasing temperatures; the former implying that the pseudogap does not arise due to proximity to superconductivity in optimally ($\approx$10%) [41] hole-doped α-Sn. Moreover, in non-optimally hole-doped samples, the tunnelling spectra display coexisting van Hove

singularity and quasiparticle peaks below and above E_F, respectively, as well as lower- (LHB) and upper (UHB) Hubbard bands near ± 0.5 eV [32,41,47]. Presently, the energy position of the Hubbard bands found in scanning tunnelling data are consistent with the shoulder features observed in photoemission (PES) [49] and angle-resolved inverse photoemission (KRIPES) [50], testifying to the electronic state probed in different tunnelling and spectroscopy experiments. However, a perusal of extant experimental data reveals high-energy electronic excitations of up to ± 1.6 eV [41] or more [49,50], which are located far beyond the reconstructed spectra derived in theory studies [32,39–41,47] of pure and doped α-Sn. Motivated be these findings, in a recent study [43] we explored the correlated many-particle problem of α-Sn, showing a large transfer of spectral weight in the one-particle spectral function of α-Sn, consistent with high-energy scanning tunneling [41,47] and spectroscopy [49,50] data. Here, motivated by a recent study [22], we unveil the role played by tunneling polarity to understand tip-assisted Mott memory phase switching in a α-Sn atomristor.

However, before presenting the potential changes of the correlated many-particle spectra of α-Sn due to electric field-induced orbital polatization [51,52] or orbital order effects [25], in Figure 2, we display a theory–experiment comparison between the total spectral function computed using the density functional and dynamical mean field theory (DFT + DMFT) [53] in ref. [43] (employing $U = 8.0$ eV and $J_H = 0.4$ eV for the on-site Coulomb interaction and the Hund's coupling, respectively), PES [49], KRIPES [50], and scanning tunneling spectroscopy (STS) data [31], showing good qualitative agreement. Particularly interesting is the peak–deep–hump pattern seen in PES and STS results below, E_F which almost coincide with the valence band DFT + DMFT spectral function. As seen, a good semiquantitative agreement with the KRIPES experimental results is also obtained. In particular, the conduction band electronic excitation at energies between 1.0 and 2.0 eV is faithfully reproduced, as a detailed form of the lineshape. Finally, also interesting is the U-shaped band gap seen in STS, which is well accounted for by the total $5p$ correlated spectral function of α-Sn, providing additional support to the multi-orbital (MO) texture of the two-dimensional Mott state of α-Sn and its analogs [22,31].

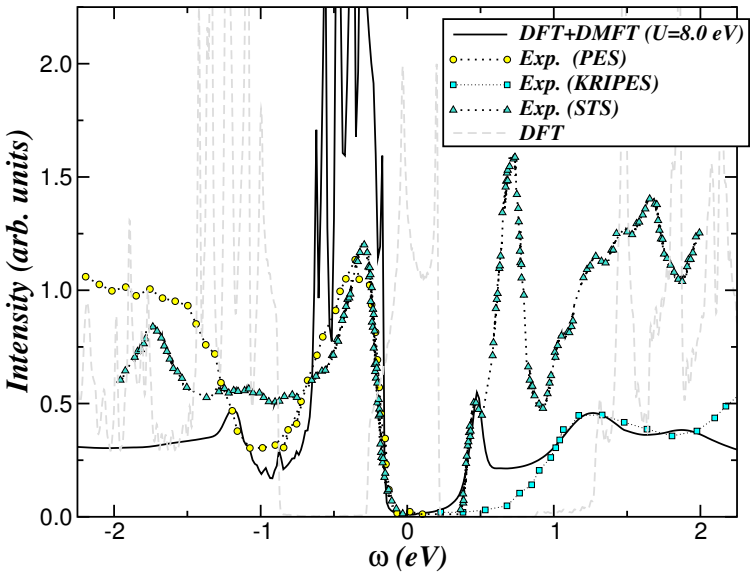

Figure 2. Theory–experiment comparison between the total DFT + DMFT density of states (DOS) of α-Sn and photoemission (PES) [49], angle-resolved inverse photoemission (KRIPES) [50], and scanning tunneling spectroscopy (STS) [31] data, showing a qualitatively good agreement: The DFT + DMFT spectral function was shifted downward by 0.08 eV to coincide with the STS curve at low energies. A particularly interesting feature is the peak–deep–hump trend in PES at binding energies of up to 1.2 eV, which is well accounted for by the total DFT + DMFT spectra obtained using $U = 8.0$ eV

and $J_H = 0.4$ eV in Ref. [43]. Notice as well the width and the shape of the Mott gap, which agrees with STS spectra [22,31]. The total DFT DOS [43] is shown for comparison.

2. Theory and Results

In this study, we adopt a correlated, many-body perspective, incorporating significant three-orbital interactions [43] in the Sn-5p shell of the α-Sn adatom adlayer. As has been demonstrated in previous DFT + DMFT studies, electronic correlations give rise to a number of intriguing physical effects when an external perturbation is introduced. The interaction of orbitals with one another naturally induces changes in orbital polarization [54,55], which in turn gives rise to a coexistence of orbital-selective metallic, insulating, and bad-metallic states. The MO DFT + DMFT [53] method is employed to elucidate the role of orbital polarization in the electronic structure reconstruction of stoichiometric ($5p^2$) α-Sn, thereby providing specific predictions for future investigations.

In a manner analogous to prior studies on MO p-band systems [56–58], the one-electron Hamiltonian for α-Sn is defined within DFT by the diagonalized $5p_a$ ($a = x, y, z$) orbitals, wherein $\epsilon_a(\mathbf{k})$represents the DFT band dispersion, which encodes for the details of the one-electron band structure of α-Sn, whose bare values are derived from the DFT spectral functions [43]. In our approach, the three $5p_a$ orbitals of α-Sn serve as the one-particle inputs for MO DFT + DMFT [53], resulting in a strongly reconstructed electronic state with increasing MO Coulomb interactions, as previously demonstrated for α-Sn [43]. In light of the significant electron correlation effects observed for α-Sn [26,40,43], it is imperative to incorporate local many-particle interactions within the MO DFT + DMFT framework to accurately describe the emergence of correlated spectral functions. These interactions include the on-site U parameter and the inter-orbital Coulomb interaction, which is given by $U' = U - 2J_H$.

In order to gain a deeper comprehension of the electric field-induced electronic structure reconstruction that is hidden in the MO problem of an α-Sn adlayer as a consequence of orbital polarization [51,52] or tunneling polarity [22] effects, we consider the orbital-dependent on-site energy term $\bar{H} = \Delta \sum_i (n_{iz\sigma} - n_{ix,y\sigma})$ in the MO Hamiltonian $H_0 + H_{int}$ of α-Sn [43]. This term acts in a manner analogous to a Zeeman field in the orbital sector [59,60], intrinsically controlling the orbital occupancy [52]. In general, the orbital field Δ [61] describes the changes in orbital polarization [51] or the ferro-orbital ordered (FOO) state within the p_x, p_y, and p_z orbitals of α-Sn under the influence of an external electric field.

The many-particle Green's function of orbital a in the $5p$ MO problem of α-Sn is computed using the $T = 0$ formulation of MO iterated-perturbation theory (MO-IPT) as an impurity solver for DMFT [62]. This perturbative, many-particle method has a proven track record of accurately describing unconventional electronic structure reconstructions induced by dynamical quantum fluctuations in broad p-band systems [56–58]. The detailed formulation of MO-IPT for correlated electrons at arbitrary fillings has already been described [62] and used in the context of extended and MO Hubbard models; therefore, we do not repeat the equations here. The MO-IPT method is computationally efficient, with real frequency output at zero and finite temperatures, enabling the study of electronic structure reconstructions of real materials. Furthermore, it provides results for the spectral functions that are in good quantitative agreement with numerical exact continuous-time quantum Monte Carlo (CT-QMC) calculations [63,64].

The electronic properties of correlated electronic materials can be modified by external perturbations such as magnetic and electric fields, which can even induce phase transitions [65]. For example, it is well established that the electronic and magnetic properties of mixed-valence perovskite manganites [66,67] are significantly influenced by orbital degrees of freedom [68,69]. The characteristics of the electronically active Mn $3d$ orbitals can be modified by interface-driven effects resulting from the breaking of surface and interface symmetry [70]. In systems with orbital-dependent degrees of freedom, a significant challenge is to achieve external and reversible control of the orbital polarization, known as

"orbitronics"; a concept proposed to understand electric field-induced orbital currents in p-doped silicon [71]. In light of prior studies that have demonstrated the ability to control orbital occupancy [52] and polarization [51] using electric fields, we present a study of the electronic structure reconstruction and orbital switching in an α-Sn atomristor induced by the orbital field Δ [59,60], which we believe to be the result of tunneling polarity effects [22].

The consideration of the orbital Zeeman field Δ was partly inspired by a study demonstrating the effects of tip-assisted phase switching and tunneling polarity on a Sn double layer grown on a Si(111) surface [22]. Additionally, our approach is motivated by the work of W. Wang et al. [72] on the photoresistive switching of a MoS_2 memristor, which demonstrated that the MoS_2 memristor could be switched by an electric field in the dark or under white light illumination through charge polarization or modulation of charge in an electric field. Moreover, our proposal is also emboldened by a DFT-based study [51] that quantified the electronic charge distribution under the influence of an electric field, utilizing polarization effects on the p-orbitals of transition-metal chalcogenides such as $Mo(Se,Te)_2$ and WSe_2. Another pertinent study [52] reported the control of orbital occupancy and switching of $3d$ orbital anisotropy in a Mn-based transition-metal oxide by an electric field. In light of these preceding studies, we investigate the role played by orbital polarization in the reconstruction of the electronic structure of the $5p$ Mott localized state of α-Sn. It should be noted that the sign of Δ has been chosen for our MO DFT + DMFT calculations in order to reflect the experimental possibility of changing the sign of the electric field through bias voltage, as well as to account for the inherent particle–hole asymmetry of the bare and correlated spectral functions of α-Sn. The interplay between particle–hole asymmetry and the sign of Δ is evident in our DFT-DMFT results for the orbital-resolved spectral functions of the α-Sn atomristor; see Figures 3 and 4.

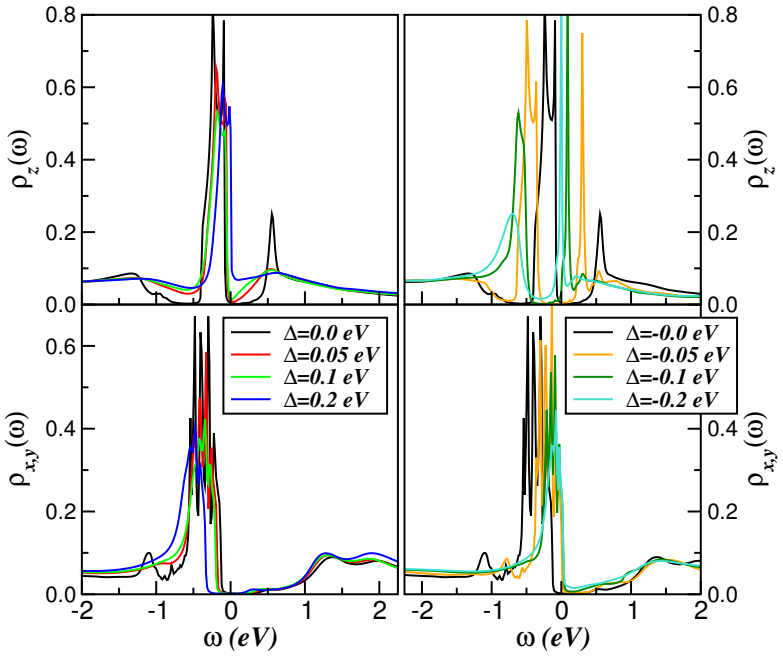

Figure 3. Local (p_a–orbital) spectral functions of α-Sn obtained for fixed total band filling of $n = 2.0$, $U = 8.0$ eV, $J_H = 0.4$ eV [43], and different values of the on-site orbital Zeeman field [59,60] Δ. Notice the sensitivity of the projected p_z density of states (PDOS) to polarity and the robustness of the planar x, y PDOS to weak orbital polarization effects.

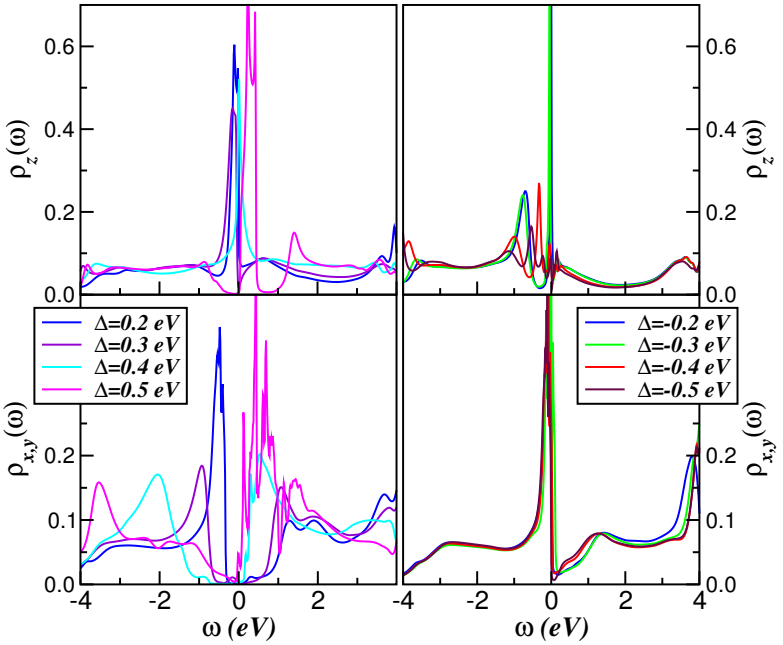

Figure 4. Energy dependence of the momentum–integrated spectral functions, showing the p_a electronic reconstruction of α-Sn when increasing the orbital Zeeman orbital field Δ. Notice the small changes in the DFT + DMFT spectral function at negative Δ values and the clearly visible electronic renormalization with coexisting metallic and insulating states at positive Δ conditions, which might be the precursor of phase change driven by a biased STM tip being used as a gating electrode [22].

Figure 3 depicts the DFT + DMFT outcomes for fixed values of $U = 8.0$ eV and $J_H = 0.4$ eV in the $5p^2$ state, with a $n = 2$ total $5p$-band filling of stoichiometric α-Sn [43]. These results are reconstructed by the application of the orbital Zeeman field Δ, where $\Delta = 0.2$ eV corresponds to a perpendicular electric field of 2.0 V/nm [73]. The left panels of Figure 3 illustrate the impact of a Zeeman field applied along an axis perpendicular to the Sn adlayer, which induces charge transfer between the $5p$ orbitals of α-Sn, thereby modifying its orbital polarization. At positive Δ values (as illustrated in the left panels of Figure 3), this charge transfer results in a modification of the orbital occupancies, leading to a relative lowering of the planar orbitals as electrons transfer from the out-of-plane orbital to the x and y orbitals. Upon switching the tunneling conditions from positive to negative bias [31], or vice versa, the opposite effect is observed in the right panels of Figure 3. A negative Δ value increases the in-plane on-site orbital energies, thereby facilitating electron flow from the x, y orbitals to the z orbital; a phenomenon that has been previously observed in other studies [51].

Although the onset of orbital polarization is relatively minor in Figure 3, a clear electronic reconstruction occurs in the p_z orbital of α-Sn at negative Δ values, as evidenced by the upper-right panel of Figure 3. The sharp conduction band edge, which peaks at 0.57 eV at zero Δ, undergoes a dynamic shift towards lower energies in proximity to the Fermi level (E_F), exhibiting an increase in intensity upon enlarging the orbital Zeeman field Δ. The electronic structure reconstruction shown in Figure 3 provides the seeds for future studies on tunneling polarity effects [22] or tip-assisted orbitronics [31] in α-Sn atomristors.

Figure 4 illustrates the evolution of the momentum-integrated spectral functions of α-Sn as the orbital Zeeman field Δ is further increased. While significant electronic reconstruction is evident at positive Δ values, the out-of-plane and planar orbitals remain relatively stable at large negative orbital Zeeman field values. This stability may be attributed to the strong particle–hole asymmetry inherent to the α-Sn parent compound, suggesting that opposite tunneling polarities could potentially induce markedly different electronic structure reconstructions. However, as illustrated in the left panels of Figure 4, all $5p$ orbitals of α-Sn undergo a discernible reshaping in the presence of positive Δ values.

The emergence of a p_z Kondo-like quasiparticle resonance [74], which was obtained at $\Delta = 0.2$ V (see Figure 3), and its narrowing before reaching Mott localization at $\Delta = 0.5$ eV, are noteworthy. An additional noteworthy aspect of the upper-left panel of Figure 4 is that the incorporation of strong dynamical correlations within DFT + DMFT partially restores the van Hove singularities in the bare DFT DOS [43], shifting them to energies slightly above the Fermi level (E_F) as the system goes towards an insulating state. Moreover, the in-plane electronic reconstruction demonstrates the persistence of Mott insulating states [75] , namely Mott localized states with varying degrees of Mott localization or Mott–Hubbard one-particle gap features across all Δ values considered in Figure 4. In summary, the results presented in Figures 3 and 4 may be pertinent to understanding or predicting tip-assisted [31] electronic reconstruction and orbital switching in α-Sn and similar materials [76]. This is due to the potential for orbital-selective metal–insulator transitions to occur as a result of the interplay between hidden particle–hole asymmetry, orbital and spin texture [77], and tunneling polarity effects.

To provide further insights into the changes in orbital polarization, Figure 5 shows the orbital occupation n_a, calculated using the orbital-resolved spectral functions of the MO Hubbard model for α-Sn. This figure illustrates the occurrence of notable changes in orbital polarization as a function of the orbital field Δ. These responses are characteristic of strongly correlated systems, wherein modifications in orbital occupations are associated with dynamic fluctuations in the reconstructed electronic state. It is noteworthy that the orbital polarization decreases with increasing Δ values up to -0.05 eV, which gives rise to changes in the correlated spectral functions, as illustrated in Figures 3 and 4. Up to this value of Δ, the results presented in Figure 5 indicate a continuous reduction in FOO due to U'–induced strong inter-orbital proximity effects, with a continuous shift in spectral weight from the z to the x, y orbital sector. Furthermore, based on the results for $\Delta > 0.2$ eV in Figure 5,we demonstrate additional orbital polarization effects. This observation, which is common to MO systems, reflects the correlation-induced rearrangement of orbitals and governs changes in the correlated electronic spectra. Due to the particle–hole asymmetry and anisotropic DFT one-particle energies and hoppings, MO correlations lead to the renormalization of the $5p$ orbitals of α-Sn in distinct ways, resulting in intrinsic orbital selectivity. Within the framework of DFT + DMFT, this orbital-selective mechanism is characterized by two distinct types of renormalization: static (MO Hartree) renormalization, which shifts the $5p$ bands in relation to one another based on their intrinsic on-site orbital energies and occupations; and the dynamic effects associated with the on-site Coulomb interactions U and U', which drive significant spectral weight transfer over a wide energy range. These findings indicate that in correlated electron systems, minor changes in the orbital field can induce considerable spectral weight transfer, thereby creating orbital-selective renormalizations of the orbital o ccupancies and one-particle spectral functions.

In order to shine light onto the interplay between orbital-selective, correlated electron physics and orbital Zeeman field effects on the changes in the $I - V$ characteristics of the α-Sn atomristor, in Figures 6 and 7, we present our results computed using the DFT + DMFT spectral functions for the different Δ values considered in Figures 3 and 4, respectively. We shall point out here that within the wide band limit of the left (L) and right (R) electrodes, the current formula for a tunnelling experiment can be written as $I = \frac{2e}{\hbar} \sum_{a\sigma} \int d\omega \, \tilde{\Gamma}(\omega) \{ f_L(\omega) - f_R(\omega) \} \rho_{a\sigma}(\omega)$ [78,79], where $\tilde{\Gamma}(\omega) = \Gamma_L(\omega)\Gamma_R(\omega)/\Gamma(\omega)$, with $\Gamma_\alpha(\omega) = \pi \sum_k |t_k^\alpha|^2 \, \delta(\omega - \varepsilon_{k\alpha})$ being the coupling strength between electrode α and the central region [80,81], and $\Gamma(\omega) = \Gamma_L(\omega) + \Gamma_R(\omega)$. $f_\alpha(\omega) = 1/(e^{\beta(\omega - \mu_\alpha)} + 1)$ and $\rho_{a\sigma}(\omega) = -\frac{1}{\pi} \mathrm{Im} \, G_{a\sigma}(\omega)$ are the Fermi function of the electrode α and the local DOS of the p_a-orbital with spin-σ of the α-Sn adatom adlayer, respectively. For simplicity, we assume a symmetric voltage drop, $\mu_L = -\mu_R = eV$, and the wide-band limit with constant DOS for the leads. Without loss of generality, these assumptions allow for a macroscopic rationalization of the orbital-resolved $I - V$ characteristics of α-Sn atomristor.

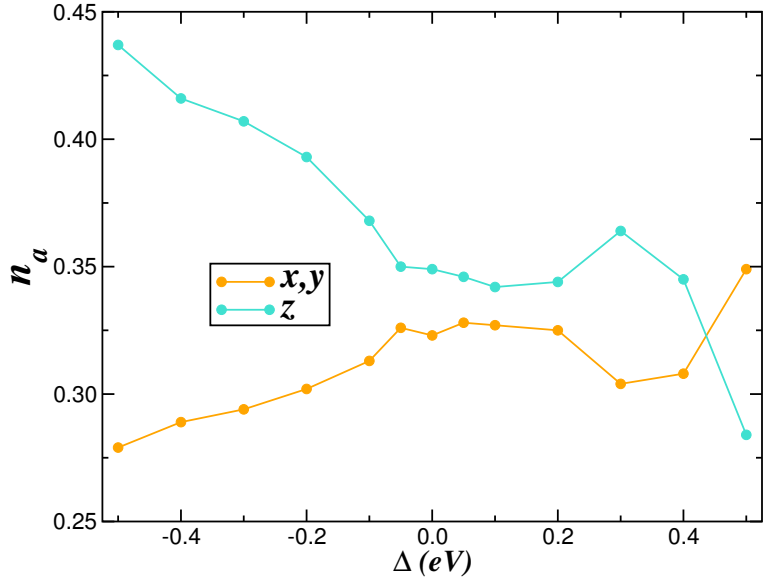

Figure 5. Illustration of the spin–resolved $5p$ orbital occupancies as a function of the orbital field Δ, indicating the reduction in the orbital polarization with increasing Δ values up to 0.1 eV and its suppression at $\Delta = 0.43$ eV.

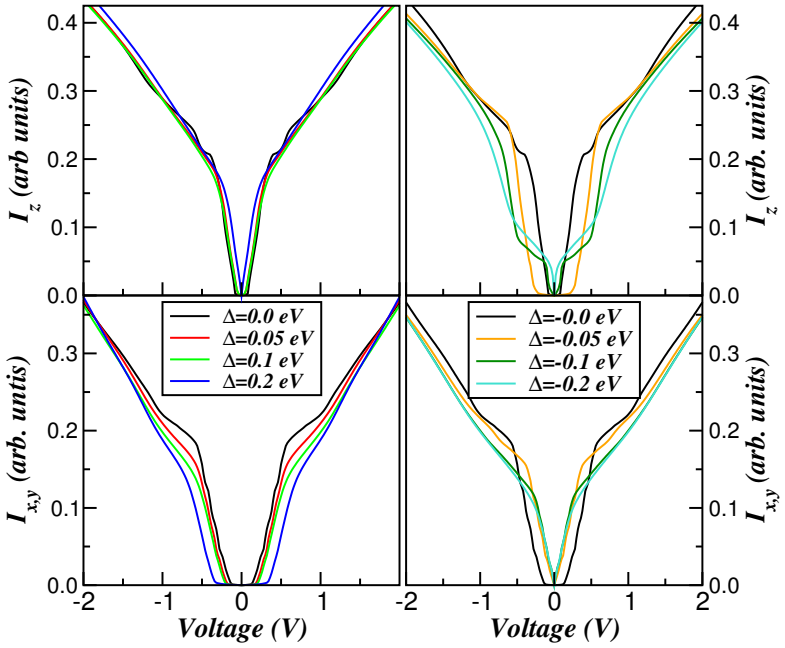

Figure 6. Evolution of the $I - V$ curves of the α-Sn atomristor device with increasing Δ values. Although volatile memory [15] is visible within the planar (x, y) orbitals at positive Δ values in the lower-left panel, an interesting feature to be seen is the nearly suppressed volatile voltage dependence in all other cases, indicating that the α-Sn atomristor exhibits orbital-selective Mott memory.

In Figures 6 and 7, we show the current–voltage $(I - V)$ characteristic curves obtained using the orbital-resolved DFT + DMFT spectral functions shown in Figures 3 and 4, respectively. As seen, with an external voltage applied across the atomristor, the resistance steady-state value changes upon changing the orbital Zeeman field Δ, indicating that the α-Sn atomristor exhibits memory. In spite of a clear orbital selectivity, in most cases, we find short-term memory to be a fingerprint of volatile memristive devices [82]. Thus, due to the selective orbital polarization process, α-Sn is predicted to exhibit an analog continuum of

resistive states owing to the changes induced in the electronic structure reconstruction, thus proving an analog memristive functionality in most of the cases shown in Figures 6 and 7. According to our results, only the p_z curves obtained at weakly negative Δ values (Figure 3 upper-right panel) displayed the nonvolatile-like memristive switching characteristics of neuromorphic nanoelectronic materials [15]. Particularly interesting in this case is the hysteresis loop present in the combined $I-V$ curves, with a clear hysteresis lobe area for applied voltages below 1.0 V. As seen in this figure, the $I-V$ characteristic curves exhibit minimal memristive behavior, which transitions to memristive switching, where the resistance steady-state value exhibts an ON/OFF ratio of 20%, assisted by orbital polarization effects. This behavior indicates that the monolayer α-Sn atomristor exhibits p_z resistive memory with a bipolar low-resistance state (LRS) and high-resistance state (HRS), as seen in experiments on the MoS_2 atomristor [16,83]. According to our DFT + DMFT results, this intrinsic bipolar switching is due to the selective orbital reconstruction, thus proving an atomristive functionality for future memory-based, brain-inspired neuromorphic computing. Although our results in Figures 6 and 7 do not show abrupt changes in the $I-V$ loops, they do indicate, however, that the sweep cycle of nonvolatile Mott memristors [4,84] might emerge upon tunable external perturbations.

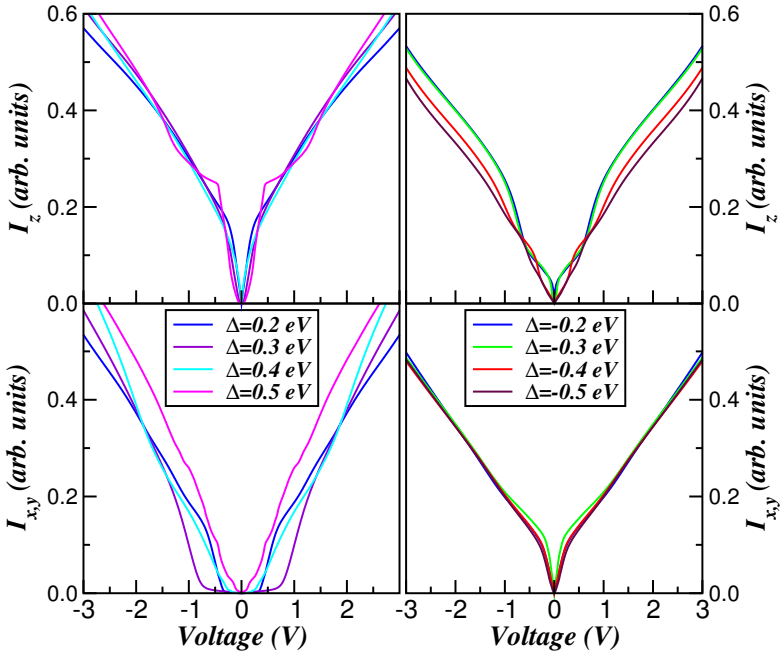

Figure 7. Evolution of the normalized-to-unit current–voltage ($I-V$) characteristics for different values of the orbital Zeeman field Δ and fixed total band filling $n=2$ of the $5p$ shell within the voltage window for the selectivity and threshold switching [22] needed for future α-Sn Mott atomristors.

3. Conclusions

To summarize, we have employed DFT + DMFT calculations to explore the effects of an orbital Zeeman field Δ in the three-orbital Hubbard model of the Sn adatom adlayer on a Si(111) surface (α-Sn). In our single-site DFT + DMFT framework, we use a Coulomb interaction parameter [43] that is capable of describing the electronic structure reconstruction seen in extant experimental data [22,31,49,50]. As we observed, this emerges due to the subtle balance between the local electron–electron interactions treated on the DMFT level and the one-particle bandwidth, which drives large-energy dynamical transfer of spectral weight. Based on our DFT + DMFT calculations, we present evidence of a correlation between induced orbital selectivity and electronic phase switching [22] in a single adatom adlayer, which is relevant to Mott memory for future neuromorphic devices using Si(111) surfaces [85]. Our current–voltage $(I-V)$ results at a finite Δ value suggest that α-Sn can be tuned into an electronic state with coexisting volatile and nonvolatile memrestive responses.

This prediction could be tested in tip-assisted morphologic studies [31] of α-Sn, which is relevant for future Mottronic devices exploiting the Mott metal–insulator transition [86].

Author Contributions: L.C., conceptualization; L.C. and S.S.C., methodology; L.C., E.F.C., S.S.C., and B.F., writing and editing. All authors have read and agreed to the published version of the manuscript.

Funding: This research received no external funding.

Data Availability Statement: The data are available upon request made to the authors.

Acknowledgments: L.C., S.S.C. and E.F.C. thank CNPq and CAPES. B.F. acknowledges Welch Professorship support from the Welch Foundation (Grant No. L-E-001-19921203) and the Texas Center for Superconductivity at the University of Houston (TcSUH). The authors also thank Laurin Craco for providing suggestions to improve the quality of the presentation in the Theory and Results section based on DeepL Write.

Conflicts of Interest: The authors declare no conflicts of interest.

References

1. Zhou, Z.; Yang, F.; Wang, S.; Wang, L.; Wang, X.; Wang, C.; Xie, Y.; Liu, Q. Emerging of two-dimensional materials in novel memristor. *Front. Phys.* **2022**, *17*, 23204. [CrossRef]
2. Li, X.-D.; Chen, N.-K.; Wang, B.-Q.; Niu, M.; Xu, M.; Miao, X.; Li, X.-B. Resistive memory devices at the thinnest limit: Progress and challengs. *Adv. Mater.* **2024**, *20*, 2307951. [CrossRef] [PubMed]
3. Song, M.-K.; Kang, J.-H.; Zhang, X.; Ji, W.; Ascoli, A.; Messaris, I.; Demirkol, A.S.; Dong, B.; Aggarwal, S.; Wan, W.; et al. Recent advances and future prospects for memristive materials, devices, and systems. *ACS Nano* **2023**, *17*, 11994. [CrossRef] [PubMed]
4. Ran, Y.; Pei, Y.; Zhou, Z.; Wang, H.; Sun, Y.; Wang, Z.; Hao, M.; Zhao, J.; Chen, J.; Yan, X. A review of Mott insulator in memristors: The materials, characteristics, applications for future computing systems and neuromorphic computing. *Nano Res.* **2023**, *16*, 1165. [CrossRef]
5. Churchland, P.S.; Sejnowski, T.J. *The Computational Brain*; The MIT Press: Cambridge, MA, USA , 1992.
6. Sagar, S.; Mohanan, K.U.; Cho, S.; Majewski, L.A.; Das, B.C. Emulation of synaptic functions with low voltage organic memtransistor for hardware oriented neuromorphic computing. *Sci. Rep.* **2022**, *12*, 3808. [CrossRef] [PubMed]
7. See also, Zidan, M.A.; Strachan, J.P.; Lu, W.D. The future of electronics based on memristive systems. *Nat. Electron.* **2018**, *1*, 22. [CrossRef]
8. Zivasatienraj, B.; Tellekamp, M.B.; Weidenbach, A.S.; Ghosh, A.; McCrone, T.M.; Doolittle, W.A. Temporal versatility from intercalation-based neuromorphic devices exhibiting 150 mV non-volatile operation. *J. Appl. Phys.* **2020**, *127*, 084501. [CrossRef]
9. Akopyan, F.; Sawada, J.; Cassidy, A.; Alvarez-Icaza, R.; Arthur, J.; Merolla, P.; Imam, N.; Nakamura, Y.; Datta, P.; Nam, G.-J.; et al. TrueNorth: Design and tool flow of a 65 mW 1 million neuron programmable neurosynaptic chip. *IEEE Trans. Comput. Aided Des. Integr. Circuits Syst.* **2015**, *34*, 1537. [CrossRef]
10. Ge, R.; Wu, X.; Kim, M.; Shi, J.; Sonde, S.; Tao, L.; Zhang, Y.; Lee, J.C.; Akinwande, D. Atomristor: Nonvolatile resistance switching in atomic sheets of transition metal dichalcogenides. *Nano Lett.* **2018**, *18*, 434. [CrossRef]
11. Wang, S.; Zhou, Z.; Yang, F.; Chen, S.; Zhang, Q.; Xiong, W.; Qu, Y.; Wang, Z.; Wang, C.; Liu, Q. All-atomristor logic gates. *Nano Res.* **2023**, *1*, 1688.
12. Beck, A.; Bednorz, J.G.; Gerber, C.; Rossel, C.; Widmer, D. Reproducible switching effect in thin oxide films for memory applications. *Appl. Phys. Lett.* **2020**, *77*, 139. [CrossRef]
13. Strukov, D.B.; Snider, G.S.; Stewart, D.R.; Williams, R.S. The missing memristor found. *Nature* **2008**, *453*, 80. [CrossRef]
14. Xu, W.; Wang, J.; Yan, X. Advances in memristor-based neural networks. *Front. Nanotechnol.* **2021**, *3*, 645995. [CrossRef]
15. Sangwan, V.K.; Hersam, M.C. Neuromorphic nanoelectronic materials. *Nat. Nanotechnol.* **2020**, *15*, 571. [CrossRef] [PubMed]
16. Kim, M.; Ge, R.; Wu, X.; Lan, X.; Tice, J.; Lee, J.C.; Akinwande, D. Zero-static power radio-frequency switches based on MoS_2 atomristors. *Nat. Commun.* **2018**, *9*, 2524. [CrossRef]
17. Bessonov, A.A.; Kirikova, M.N.; Petukhov, D.I.; Allen, M.; Ryhänen, T.; Bailey, M.J.A. Layered memristive and memcapacitive switches for printable electronics. *Nat. Mater.* **2014**, *14*, 199. [CrossRef]
18. Son, D.; Chae, S.I.; Kim, M.; Choi, M.K.; Yang, J.; Park, K.; Kale, V.S.; Koo, J.H.; Choi, C.; Lee, M.; et al. Colloidal synthesis of uniform-sized molybdenum disulfide nanosheets for wafer-scale flexible nonvolatile memory. *Adv. Matter* **2016**, *28*, 9326. [CrossRef]
19. Quian, K.; Tay, R.Y.; Nguyen, V.C.; Wang, J.; Cai, G.; Chen, T.; Teo, E.H.T.; Lee, P.S. Hexagonal boron nitride thin film for flexible resistive memory applications. *Adv. Func. Mater.* **2016**, *26*, 2176. [CrossRef]
20. Pan, C.; Ji, Y.; Xiao, N.; Hui, F.; Tang, K.; Guo, Y.; Xie, X.; Puglisi, F.M.; Larcher, L.; Miranda, E.; et al. Coexistence of grain-boundaries-assisted bipolar and threshold resistive switching in multilayer hexagonal boron nitride. *Adv. Func. Mater.* **2017**, *27*, 1604811. [CrossRef]

21. Tan, C.; Zhang, H. Two-dimensional transition metal dichalcogenide nanosheet-based composites. *Chem. Soc. Rev.* **2015**, *44*, 2713. [CrossRef]
22. Ming, F.; Snijders, P.C.; Weitering, H.H. Controlled switching of bistable nanophase domains on a silicon surface. *ACS Nano* **2023**, *17*, 11914. [CrossRef] [PubMed]
23. Chua, L.O. Memristor-The missing circuit element. *IEEE Trans. Circuit Theory* **1971**, *18*, 507. [CrossRef]
24. Tosatti, E.; Anderson, P. W. Charge and spin density waves on semiconductor surfaces. *Jpn. J. Appl. Phys.* **1974**, *13*, 381. [CrossRef]
25. Kim, H.; Yoshida, Y.; Lee, C.-C.; Chang, T.-R.; Jeng, H.-T.; Lin, H.; Haga, Y.; Fisk, Z.; Hasegawa, Y. Atomic-scale visualization of surface-assisted orbital order. *Sci. Adv.* **2017**, *3*, eaao0362. [CrossRef]
26. Profeta, G.; Tosatti, E. Triangular Mott-Hubbard Insulator Phases of Sn/Si(111) and Sn/Ge(111) Surfaces. *Phys. Rev. Lett.* **2007**, *98*, 086401. [CrossRef] [PubMed]
27. Brihuega, I.; Custance, O.; Pérez, R.; Gómez-Rodríguez, J.M. Intrinsic character of the (3×3) to $(\sqrt{3} \times \sqrt{3})$ phase transition in Pb/Si(111). *Phys. Rev. Lett.* **2005**, *94*, 046101. [CrossRef] [PubMed]
28. Cortés, R.; Tejeda, A.; Lobo-Checa, J.; Didiot, C.; Kierren, B.; Malterre, D.; Merino, J.; Flores, F.; Michel, E.G.; Mascaraque, A. Competing charge ordering and Mott phases in a correlated Sn/Ge(111) two-dimensional triangular lattice. *Phys. Rev. B* **2013**, *88*, 125113. [CrossRef]
29. Glass, S.; Li, G.; Adler, F.; Aulbach, J.; Fleszar, A.; Thomale, R.; Hanke, W.; Claessen, R.; Schäfer, J. Triangular spin-orbit-coupled lattice with strong Coulomb correlations: Sn atoms on a SiC(0001) substrate. *Phys. Rev. Lett.* **2015**, *114*, 247602. [CrossRef]
30. Yi, S.; Lee, H.; Choi, J.-H.; Cho, J.-H. Nature of the insulating ground state of the two-dimensional Sn atom lattice on SiC(0001). *Sci. Rep.* **2016**, *6*, 30598. [CrossRef]
31. Ming, F.; Mulugeta, D.; Tu, W.; Smith, T.S.; Vilmercati, P.; Lee, G.; Huang, Y.-T.; Diehl, R.D.; Snijders, P.C.; Weitering, H.H. Hidden phase in a two-dimensional Sn layer stabilized by modulation hole doping. *Nat. Comm.* **2016**, *8*, 14721. [CrossRef]
32. Wu, X.; Ming, F.; Smith, T.S.; Liu, G.; Ye, F.; Wang, K.; Johnston, S.; Weitering, H.H. Superconductivity in a hole-doped Mott-insulating triangular adatom layer on a silicon surface. *Phys. Rev. Lett.* **2020**, *125*, 117001. [CrossRef]
33. Ming, F.; Wu, X.; Chen, C.; Wang, K.D.; Mai, P.; Maier, T.A.; Strockoz, J.; Venderbos, J.W.F.; González, C.; Ortega, J.; et al. Evidence for chiral superconductivity on a silicon surface. *Nat. Phys.* **2023**, *19*, 500. [CrossRef]
34. Carpinelli, J.M.; Weitering, H.H.; Plummer, E.W.; Stumpf, R. Direct observation of a surface charge density wave. *Nature* **1996**, *381*, 398. [CrossRef]
35. Matetskiy, A.V.; Denisov, N.V.; Hsing, C.R.; Wei, C.M.; Zotov, A.V.; Saranin, A.A. Observation of the nesting and defect-driven 1D incommensurate charge density waves phase in the 2D system. *J. Phys. Condens. Mat.* **2019**, *31*, 115402. [CrossRef]
36. Adler, F.; Rachel, S.; Laubach, M.; Maklar, J.; Fleszar, A.; Schäfer, J.; Claessen, R. Correlation-driven charge order in a frustrated two-dimensional atom lattice. *Phys. Rev. Lett.* **2019**, *123*, 086401. [CrossRef]
37. Li, G.; Laubach, M.; Fleszar, A.; Hanke, W. Geometrical frustration and the competing phases of the Sn/Si(111) $(\sqrt{3} \times \sqrt{3}R30^\circ)$ surface systems. *Phys. Rev. B* **2011**, *83*, 041104. [CrossRef]
38. Li, G.; Höpfner, P.; Schäfer, J.; Blumenstein, C.; Meyer, S.; Bostwick, A.; Rotenberg, E.; Claessen, R.; Hanke, W. Magnetic order in a frustrated two-dimensional atom lattice at a semiconductor surface. *Nat. Commun.* **2013**, *4*, 1620. [CrossRef] [PubMed]
39. Schuwalow, S.; Grieger, D.; Lechermann, F. Realistic modeling of the electronic structure and the effect of correlations for Sn/Si(111) and Sn/Ge(111) surfaces. *Phys. Rev. B* **2010**, *82*, 035116. [CrossRef]
40. Hansmann, P.; Ayral, T.; Vaugier, L.; Werner, P.; Biermann, S. Long-range Coulomb interactions in surface systems: A first-principles description within self-consistently combined *GW* and dynamical mean-field theory. *Phys. Rev. Lett.* **2013**, *110*, 166401. [CrossRef]
41. Ming, F.; Johnston, S.; Mulugeta, D.; Smith, T.S.; Vilmercati, P.; Lee, G.; Maier, T.A.; Snijders, P.C.; Weitering, H.H. Realization of a hole-doped Mott insulator on a triangular silicon lattice.*Phys. Rev. Lett.* **2017**, *119*, 266802. [CrossRef]
42. Wolf, S.; Di Sante, D.; Schwemmer, T.; Thomale, R.; Rachel, S. Triplet superconductivity from nonlocal Coulomb repulsion in an atomic Sn layer Deposited onto a Si(111) substrate. *Phys. Rev. Lett.* **2022**, *128*, 167002. [CrossRef] [PubMed]
43. Craco, L.; Carara, S.S. Orbital selectivity in Sn adatom adlayer on a Si(111) surface. *Europhys. Lett.* **2024**, *145*, 26003. [CrossRef]
44. McChesney, J.L.; Bostwick, A.; Ohta, T.; Seyller, T.; Horn, K.; González, J.; Rotenberg, E. Extended van Hove singularity and superconducting ionstability in doped graphene. *Phys. Rev. Lett.* **2010**, *104*, 136803. [CrossRef] [PubMed]
45. Craco, L. Electronic properties of normal and extended Hubbard model for bilayer cuprates. *Eur. Phys. J. B* **2022**, *95*, 125. [CrossRef]
46. Gneist, N.; Classen, L.; Scherer, M.M. Competing instabilities of the extended Hubbard model on the triangular lattice: Truncated-unity functional renormalization group and application to moiré materials. *Phys. Rev. B* **2022**, *106*, 125141. [CrossRef]
47. Ming, F.; Smith, T.S.; Johnston, S.; Snijders, P.C.; Weitering, H.H. Zero-bias anomaly in nanoscale hole-doped Mott insulators on a triangular silicon surface. *Phys. Rev. B* **2018**, *97*, 075403. [CrossRef]
48. Xiong, Y.-L.; Guan, J.-Q.; Wang, R.-F.; Song, C.-L.; Ma, X.-C.; Xue, Q.-K. Experimental observation of pseudogap in a modulation-doped Mott insulator: Sn/Si(111)-$(\sqrt{3} \times \sqrt{3})R30^\circ$. *Chin. Phys. B* **2022**, *31*, 067401. [CrossRef]
49. Modesti, S.; Petaccia, L.; Ceballos, G.; Vobornik, I.; Panaccione, G.; Rossi, G.; Ottaviano, L.; Larciprete, R.; Lizzit, S.; Goldoni, A. Insulating Ground State of $(\sqrt{3} \times \sqrt{3})R30^\circ$. *Phys. Rev. Lett.* **2007**, *98*, 126401. [CrossRef] [PubMed]
50. Charrier, A.; Pérez, R.; Thibaudau, F.; Debever, J.-M.; Ortega, J.; Flores, F.; Themlin, J.-M. Contrasted electronic properties of Sn-adatom-based $(\sqrt{3} \times \sqrt{3})R30^\circ$ reconstructions on Si(111). *Phys. Rev. B* **2001**, *64*, 115407. [CrossRef]

51. Belviso, F.; Cammarata, A.; Missaoui, J.; Polcar, T. Effect of electric fields in low-dimensional materials: Nanofrictional response as a case study. *Phys. Rev. B* **2020**, *102*, 155433. [CrossRef]
52. Preziosi, D.; Alexe, M.; Hesse, D.; Salluzzo, M. Electric-field control of the orbital occupancy and magnetic moment of a transition-metal oxide. *Phys. Rev. Lett.* **2015**, *115*, 157401. [CrossRef]
53. Kotliar, G.; Savrasov, S.Y.; Haule, K.; Oudovenko, V.S.; Parcollet, O.; Marianetti, C.A. Electronic structure calculations with dynamical mean-field theory. *Rev. Mod. Phys.* **2006**, *78*, 865. [CrossRef]
54. Werner, P.; Millis, A.J. High-spin to low-spin and orbital polarization transitions in multiorbital Mott systems. *Phys. Rev. Lett.* **2007**, *99*, 126405. [CrossRef]
55. Ni,Y.; Quan, Y.-M.; Liu, J.; Song, Y.; Zou, L.J. Electronic correlation-driven orbital polarization transitions in the orbital-selective Mott compound $Ba_2CuO_{4-\delta}$. *Phys. Rev. B* **2021**, *103*, 214510. [CrossRef]
56. Craco, L.; Leoni, S. Bulk quantum correlations and doping-induced nonmetallicity in the Bi_2Se_3 topological insulator. *Phys. Rev. B* **2012**, *85*, 075114. [CrossRef]
57. Craco, L.; Leoni, S. Tunable Kondo-Mott physics in bulk Bi_2Te_2Se topological insulator. *Phys. Rev. B* **2012**, *85*, 195124. [CrossRef]
58. Craco, L.; Leoni, S. Magnetoresistance in the spin-orbit Kondo state of elemental bismuth. *Sci. Rep.* **2015**, *5*, 13772. [CrossRef]
59. Nagai, Y. Robust superconductivity with nodes in the superconducting topological insulator $Cu_xBi_2Se_3$: Zeeman orbital field and nonmagnetic impurities. *Phys. Rev. B* **2015**, *91*, 060502. [CrossRef]
60. Zhao, H.J.; Wang, Y.; Yang, Y.; Ma, Y.; Bellaiche, L. Zeeman-type energy level splittings controlled by an electric field. *Phys. Rev. B* **2022**, *106*, 024104. [CrossRef]
61. Craco, L.; Laad, M.S.; Leoni, S. Microscopic description of insulator-metal transition in high-pressure oxygen. *Sci. Rep.* **2017**, *7*, 2632. [CrossRef]
62. Craco, L. Quantum orbital entanglement: A view from the extended periodic Anderson model. *Phys. Rev. B* **2008**, *77*, 125122. [CrossRef]
63. Craco, L.; Leoni, S. Theory of two-fluid metallicity in superconducting FeSe at high pressure. *Phys. Rev. B* **2019**, 100, 121101. [CrossRef]
64. Craco, L. Orbital-selective electronic localization in dimerized NbO_2: From Peierls to Mott. *Phys. Rev. B* **2024**, *109*, 235136. [CrossRef]
65. Ahn, C.H.; Triscone, J.-M.; Mannhart, J. Electric field effect in correlated oxide systems. *Nature* **2003**, *424*, 1015. [CrossRef] [PubMed]
66. Coey, J.M.D.; Viret, M.; von Molnár, S. Mixed-valence manganites. *Adv. Phys.* **1999**, 48, 167. [CrossRef]
67. De Luca, G.M.; Perroni, C.A.; Di Capua, R.; Cataudella, V.; Chiarella, F.; Minola, M.; Brookes, N.B.; Salluzzo, M.; Ghiringhelli, G. Strain and electric field control of the orbital and spin order in multiferroic $BiMnO_3$. *Eur. Phys. J. Plus* **2020**, *135*, 473. [CrossRef]
68. Tokura, Y.; Nagaosa, N. Orbital physics in transition-metal oxides. *Science* **2000**, *288*, 462. [CrossRef] [PubMed]
69. Laad, M.S.; Craco, L.; Müller-Hartmann, E. Role of orbital degeneracy in double-exchange systems. *Phys. Rev. B* **2001**, *63*, 214419. [CrossRef]
70. Pesquera, D.; Herranz, G.; Barla, A.; Pellegrin, E.; Bondino, F.; Magnano, E.; Sánchez, F.; Fontcuberta, J. Surface symmetry-breaking and strain effects on orbital occupancy in transition metal perovskite epitaxial films. *Nat. Commun.* **2012**, *3*, 1189. [CrossRef]
71. Bernevig, B.A.; Hughes, T.L.; Zhang, S.-C. Orbitronics: The intrinsic orbital current in *p*-doped silicon. *Phys. Rev. Lett.* **2005**, *95*, 066601. [CrossRef]
72. Wang, W.; Panin, G.N.; Fu, X.; Zhang, L.; Ilanchezhiyan, P.; Pelenovich, V.O.; Fu, D.; Kang, T.W. MoS_2 memristor with photoresistive switching. *Sci. Rep.* **2016**, *6*, 31224. [CrossRef] [PubMed]
73. Craco, L.; Carara, S.S.; Leoni, S. Interplay of electric field and disorder in Dirac liquid silicene. *Eur. Phys. J. B* **2021**, *94*, 47. [CrossRef]
74. Georges, A.; Kotliar, G.; Krauth, W.; Rozenberg, M.J. Dynamical mean-field theory of strongly correlated fermion systems and the limit of infinite dimensions. *Rev. Mod. Phys.* **1996**, *68*, 13. [CrossRef]
75. Deng, X.; Mravlje, J.; Žitko, R.; Ferrero, M.; Kotliar, G.; Georges, A. How bad metals turn good: Spectroscopic signatures of resilient quasiparticles. *Phys. Rev. Lett.* **2013**, *110*, 086401. [CrossRef] [PubMed]
76. Vandelli, M.; Galler, A.; Rubio, A.; Lichtenstein, A.I.; Biermann, S.; Stepanov, E.A. Doping-dependent charge- and spin-density wave orderings in a monolayer of Pb adatoms on Si(111). *npj Quantum Mater.* **2024**, *9*, 19. [CrossRef]
77. Jäger, M.; Brand, C.; Weber, A.P.; Fanciulli, M.; Dil, J.H.; Pfnür, H.; Tegenkamp, C. α-Sn phase on Si(111): Spin texture of a two-dimensional Mott state. *Phys. Rev. B* **2018**, *98*, 165422. [CrossRef]
78. Meir, Y.; Wingreen, N.S. Landauer formula for the current through an interacting electron region. *Phys. Rev. Lett.* **1992**, *68*, 2512. [CrossRef]
79. Craco, L.; Kang, K. Perturbation treatment for transport through a quantum dot. *Phys. Rev. B* **1999**, *59*, 12244. [CrossRef]
80. Cuniberti, G.; Craco, L.; Porath, D.; Dekker, C. Backbone-induced semiconducting behavior in short DNA wires. *Phys. Rev. B* **2002**, *65*, 241314. [CrossRef]
81. Bao, X.-X.; Wang, X.-F. Effects of long-range dispersive interaction on the electron transport in short single strands of guanine bases. *Int. J. Quantum Chem.* **2023**, *1*, e27251. [CrossRef]

82. Greenlee, J.D.; Shank, J.C.; Tellekamp, M.B.; Gunning, B.P.; Fabien, C.A.M.; Doolittle, W.A. Liquid phase electro-epitaxy of memristive $LiNbO_2$ crystals. *Cryst. Growth Des.* **2014**, *14*, 2218. [CrossRef]
83. Tang, B.; Veluri, H.; Li, Y.; Yu, Z.G.; Waqar, M.; Leong, J.F.; Sivan, M.; Zamburg, E.; Zhang, Y.-W.; Wang, J.; et al. Wafer-scale solution-processed 2D material analog resistive memory array for memory-based computing. *Nat. Comms.* **2022**, *13*, 3037. [CrossRef] [PubMed]
84. Liu, X.; Nandi, S.K.; Venkatachalam, D.K.; Belay, K.; Song, S.; Elliman, R.G. Reduced threshold current in NbO_2 selector by engineering device structure. *IEEE Electron Device Letts.* **2014**, *35*, 1055. [CrossRef]
85. Zhou, Y.; Ramanathan, S. Mott memory and neuromorphic devices. *Proc. IEEE* **2015**, *103*, 1289. [CrossRef]
86. Tokura, Y.; Kawasaki, M.; Nagaosa, N. Emergent functions of quantum materials. *Nat. Phys.* **2017**, *13*, 1056. [CrossRef]